State-selective single- and double-electron-capture processes in slow Ar^{8+}-He collisions

Md Abul Kalam Azad Siddiki [ORCID],[1] Guopeng Zhao [ORCID],[2] Ling Liu,[3,*] and Deepankar Misra [ORCID][1,†]

[1]*Department of Nuclear and Atomic Physics, Tata Institute of Fundamental Research, Homi Bhabha Road, Colaba, Mumbai 400005, India*
[2]*College of Data Science, Jiaxing University, Jiaxing 314001, China*
[3]*Key Laboratory of Computational Physics, Institute of Applied Physics and Computational Mathematics, Beijing 100088, China*

We present an experiment with numerical simulations for the state-selective single-electron-capture process in low-energy 1–8-keV/u Ar^{8+}-He collisions. The relative cross sections for the state-selective transitions are obtained from the measured Q-value spectra. Subshell-resolved differential scattering angle distributions (DSADs) for the dominant ($n = 4$) $1s$ to $4s$, $4p$, $4d$, and $4f$ transitions and weak ($n = 5$) $1s$ to $5s$ and $5p$ transitions at 1 keV/u and some mixed state transitions for 5- and 8-keV/u collision energy are measured. The experimentally obtained state-selective DSADs are compared with the two-center atomic orbital close-coupling calculations and qualitatively reproduced the oscillatory structures, which are quantum in nature. Undulations in the small scattering angles for $1s$ to $4s$ and $4p_0$ transitions are found to be arising from quantum matter-wave scattering, further satisfied by the simple mathematical model based on the optical Fraunhofer diffraction theory of light. The double differential Q-value versus scattering angle distributions give insight into the double-electron-capture mechanisms measured at 5- and 8-keV/u collision energies. Our findings shed light on the excited-state electronic dynamics to characterize the highly charged ion-atom collisions in the highly perturbative regime.

I. INTRODUCTION

Electron capture (EC) or charge exchange is the dominant process in collisions of highly charged ions (HCIs) with neutral atoms, molecules, and clusters in low- and intermediate-energy collisions [1–4]. In electron-capture collisions, one or more target electrons are captured into the excited states of the projectiles. The subsequent deexcitation of these excited states through photon emissions leads to photon spectra in extreme ultraviolet to soft-x-ray regimes [5]. The origin of the soft x rays emitted from comets sheds light on the primary EC process between the solar wind HCIs and the comet's atmosphere entities [5]. The EC process also plays an important role in diagnosing fusion and astrophysical plasmas [6,7]. If more than one electron is captured into the excited states of the projectile, it leads to the relaxation of excited states through the autoionization process or radiative decay, which is a general feature of HCI-atom or -molecule collisions (see, e.g., Refs. [2,3,8]). The electron-capture process also draws much attention to solving the fundamental scattering problems for few-body momentum exchanges [9,10]. In this regard, various theoretical models, such as molecular orbital close coupling [11,12], atomic orbital close coupling (AOCC) [13,14], and numerical solution of the time-dependent Schrodinger equation [15], have been developed to study the quantum state selectivity of the EC process and differential cross sections to get insight into the ongoing collision dynamics.

With the advent of three-dimensional momentum imaging techniques such as cold target recoil ion momentum spectroscopy (COLTRIMS) [16,17], $n\ell$-selective (where n and ℓ are the principal quantum number and angular quantum number, respectively) measurements have been carried out for a wide range of collision energy (e.g., keV to MeV) [18,19]. The obtained $n\ell$-resolved Q-value (where Q is the system inelasticity) spectrum gives access to the reaction window of the collisions. At the same time, the state-selective differential scattering angle distributions (DSADs) imprint the ongoing collision dynamics. In these slow collisions, a quasimolecular ion is formed, manifesting the different dynamical couplings' (e.g., radial and rotational couplings) effect through the coupling between the intermediate molecular states with the same or different symmetries [14,20]. The magnetic quantum number (m) selective differential cross sections encoded the information about the dynamical couplings, which arise geometrically from the rotation of the molecular orbitals with respect to the internuclear axis of the quasimolecular ion. The molecular orbital alignment effects have been investigated in several studies, which also involve optically prepared excited states of the target [21,22].

In the electron-capture process, the capture probability is defined by the distributions of the transition probability as a function of the impact parameter (b). The scattering of the projectiles within the impact parameter b range is analogous to the optical Fraunhofer-type diffraction where light is diffracted by the aperture. Following the pioneering work by van der Poel *et al.* [23,24] on the atomic matter-wave diffraction for Li$^+$-Na single-electron-capture (SC) collisions, a few more studies have been reported in low-intermediate-high energy ion-atom collisions [19,25–28].

---

*Contact author: liu_ling@iapcm.ac.cn
†Contact author: dmisra@tifr.res.in

For HCI-atom collisions, the Ar^{8+} projectile has a unique advantage for its well-separated energy levels for the different $n\ell$ states, which are possible to resolve experimentally using supersonic gas jet target (e.g., He and H_2) [18,29]. In low-energy Ar^{8+}-He SC collisions, the state-selective DSADs have been investigated both experimentally and theoretically for $1s$ to $4s$, $4p$, and mixed $4d+4f$ transitions [14,18,30]. However, little attention has been given to $1s$ to $n\ell = 5\ell$ transitions, which also contribute as collision energy increases. The state-selective DSADs will shed light on the collision dynamics for the highly excited $n\ell$ transitions. Earlier, Bliman *et al.* [31] studied the Ar^{8+}-He double-electron-capture (DC) process using the translational energy gain spectroscopy and reported the DC into the projectile final states with lower Q values (<85 eV). However, there is a lack of experimental data for the channels with higher Q values, i.e., the projectile captures both electrons into the lower projectile states. Recently, Zhang *et al.* [32] calculated the partial cross sections of the projectile final states ($n'\ell'n\ell$) for the DC process at 0.1- to 100-keV/u collision energies using the two-active semiclassical asymptotic-state close-coupling approach. The Coulomb potential-energy curves (CPECs) give access to the classical electron-capture radii and the classical deflection angles for the single-step and double-step electron-capture processes. The state-selective DSADs give insight into the different double-electron-capture mechanisms.

In this paper, we study the state-selective electron-capture processes in 1–8-keV/u Ar^{8+}-He collisions. The experimentally measured state-selective DSADs ($n\ell = 4\ell$ and 5ℓ states) are compared with the two-center atomic orbital close-coupling (TC-AOCC) calculations. The TC-AOCC calculations qualitatively reproduce the dominant oscillatory structures in the measured DSADs arising from the coherent oscillations. A simple mathematical model based on the Fraunhofer diffraction theory (FDT) indicates that the undulations in the smaller scattering angles arise from the projectile matter-wave scattering. The doubly differential Q-value vs scattering angle distributions shed light on the double-electron-capture mechanisms.

The paper is organized as follows: In Sec. II, we briefly describe experimental methods. In Sec. III, a short description of the TC-AOCC method is given. The state-selective relative cross sections, a detailed discussion about the DSADs for SC, and the nature of electron-capture mechanisms for DC are given in Sec. IV. Finally, in Sec. V, we conclude our major findings. In the following, atomic units are used throughout unless otherwise indicated.

II. EXPERIMENT

The experiments were performed in the electron cyclotron resonance-based ion accelerator (ECRIA) [33] facility at Tata Institute of Fundamental Research, Mumbai, using a COLTRIMS reaction microscope [34,35]. The 1-, 5-, and 8-keV/u Ar^{8+} projectile beam interacts perpendicularly with the supersonic He gas jet. The supersonic gas jet has been produced by expanding the He gas of a stagnation pressure 2 bars through a 30-μm nozzle towards the source vacuum chamber (base pressure $\simeq 2 \times 10^{-8}$ mbar) followed by a double-stage skimmer assembly. A cylindrical electrostatic

beam cleaner has been used to avoid the primary projectile beam contamination owing to the electron capture from the residual gases in the long beamline. The recoil ions and the charge-changing projectiles are coincidentally detected by combining the COLTRIMS reaction microscope with a final projectile charge state analyzer. The electric fields in the extraction and acceleration regions were 5.33 and 7.77 V/cm, respectively. Both recoil and projectile detector assembly have the combination of an 80-mm-diameter microchannel plate followed by the position-sensitive delay line anode. The beam current at the final Faraday cup has been maintained at around 100 pA. The data are stored in an event-by-event list mode using the COBOLDPC software for offline analysis. Details of the three-dimensional momentum calculation can be found elsewhere [34,36].

The momentum exchange due to the electron being captured by the projectile is compensated by the relative motion between the target and the projectile. Using the energy and momentum conservation, one can easily deduce the following relations of longitudinal ($p_{r\parallel}$) and transverse ($p_{r\perp}$) recoil momentum and the corresponding scattering angle (θ):

$$p_{r\parallel} = -\frac{n_e v}{2} - \frac{Q}{v}, \qquad (1)$$

$$p_{r\perp} = p_{p\perp}, \qquad (2)$$

$$\theta = \frac{p_{p\perp}}{p_{ip}}, \qquad (3)$$

where $Q = E_{\text{binding}p} - E_{\text{binding}t}$, n_e, v, and p_{ip} are the binding-energy differences (i.e., system inelasticity) of the captured electron between the final projectile state and the initial target state, number of captured electrons, projectile velocity, and incoming projectile momentum, respectively. From the experimental data, we have information about the $p_{r\parallel}$ and $p_{r\perp}$ for each event.

The SC and DC processes are analyzed with the time-of-flight gates in coincidence with the scattered projectiles.

III. THEORY

The TC-AOCC method for dealing with heavy particle collisions is described in detail in Refs. [9,14,37]. Here, we have given a brief description. The electronic Hamiltonian for the single-active electron Ar^{8+}-He collision system can be expressed as

$$H = -\frac{1}{2}\nabla_r^2 + V_A(r_A) + V_B(r_B), \qquad (4)$$

where $V_A(r_A)$ and $V_B(r_B)$ represent the electron interaction with the projectile core (Ar^{8+}) and target core (He^+), respectively.

The model potentials from Ref. [18] are used for V_A and V_B as follows:

$$V_A(r) = -\frac{8}{r} - \frac{10}{r}\exp(-5.50r) - 5.50\exp(-5.50r), \quad (5)$$

$$V_B(r) = -\frac{1}{r} - \frac{1}{r}\exp(-2.69697r)$$
$$- 0.65354\exp(-2.69697r). \qquad (6)$$

For the He target, the above model potential can produce an accurate ionization energy of He^+.

The angle-differential cross sections for the $i \rightarrow j$ transition can be obtained by

$$\frac{d\sigma_{ij}}{d\theta} = 2\pi \sin\theta |A_{ji}|^2, \qquad (7)$$

where the scattering amplitudes A_{ji} are determined by the impact parameter dependent transition amplitudes and are given by

$$A_{ji}(\theta) = \gamma \int_0^{+\infty} bF(b)J_{|m_j - m_i|}\left[2b\mu\upsilon \sin\frac{\theta}{2}\right]db. \qquad (8)$$

Here

$$F(b) = a_{ji}e^{2(i/\upsilon)Z_T Z_P \ln b}, \qquad (9)$$

$\gamma = \mu\upsilon(-i)^{|m_f - m_i|+1}$, μ is the reduced mass of the projectile and target, and $m_j(m_i)$ represents the magnetic quantum number of the final (initial) state. The function J represents the first kind of Bessel function. For a given impact parameter b the transition amplitude a_{ji} is calculated. The eikonal phase (or Coulomb phase) due to the Coulomb repulsion between the target and the projectile nuclei is defined as $e^{2(i/\upsilon)Z_T Z_P \ln b}$, where Z_T and Z_P are the corresponding effective charges for the projectile and target cores.

IV. RESULTS AND DISCUSSION

A. $n\ell$-resolved relative cross sections

In the 1-keV/u Ar^{8+}-He SC process, the $1s$ to $4s$, $4p$, $4d$, $4f$, $5s$, and $5p$ transitions [see Fig. 1(a)] are resolved experimentally. For the dominant $n = 4$ shell, the distribution is maximized for the $4d$ state, and $4p$ is the second most dominant state. The contributions are much less for the other two $4s$ and $4f$ states. The populations are statistically distributed in the middle $\ell=1$ and 2 states and decrease for the $\ell=0$ and 3 states. For the weak $n=5$ shell, the $1s$ to $5s$ transition is dominant over the $1s$ to $5p$ transition. The other $5d + 5f + 5g$ states are almost negligible. Very small contributions to the transfer excitation (TE) channels like [$3s$, $He^+(n = 2)$], [$3s$, $He^+(n = 3)$], [$3s$, $He^+(n = 4)$], and [$3p$, $He^+(n = 2)$] have been observed [see Fig. 1(a), inset]. The [$3s$, $He^+(n = 2)$] channel is mixed with the $3d$ channel as both have similar Q values. The small yields of the TE channels indicate the second electron is almost frozen during the collisions in these highly perturbative collisions. For 5- and 8-keV/u collision energies, $1s$ to $4s$, $4p$, $4d+4f$, $5s+5p$, and $5d + 5f + 5g$ transitions are resolved experimentally [see Figs. 1(b) and 1(c)]. The $4d+4f$ channel is the dominant SC channel. A small contribution from the $1s$ to $3d$ transition has been observed, which has increased with the increment of the collision energy. This could be understood as the width of the reaction window is proportional to the square root of collision velocity (i.e., $\Delta E \propto \upsilon^{0.5}$). A minor contribution from the [$3p$, $He^+(n = 2)$] TE channel has also been observed. The large Q values associated with these channels (e.g., $3d$ and TE channels) require small capture radii in order to capture the electrons. These small impact parameters result in a lower cross section of these channels, and also these states lie far away from the mean of the reaction window (≈ 25.9 eV). The relative yields of the SC channels are tabulated in Table I. The relative yields between the [$3p$, $He^+(n = 2)$] and $3d$ states
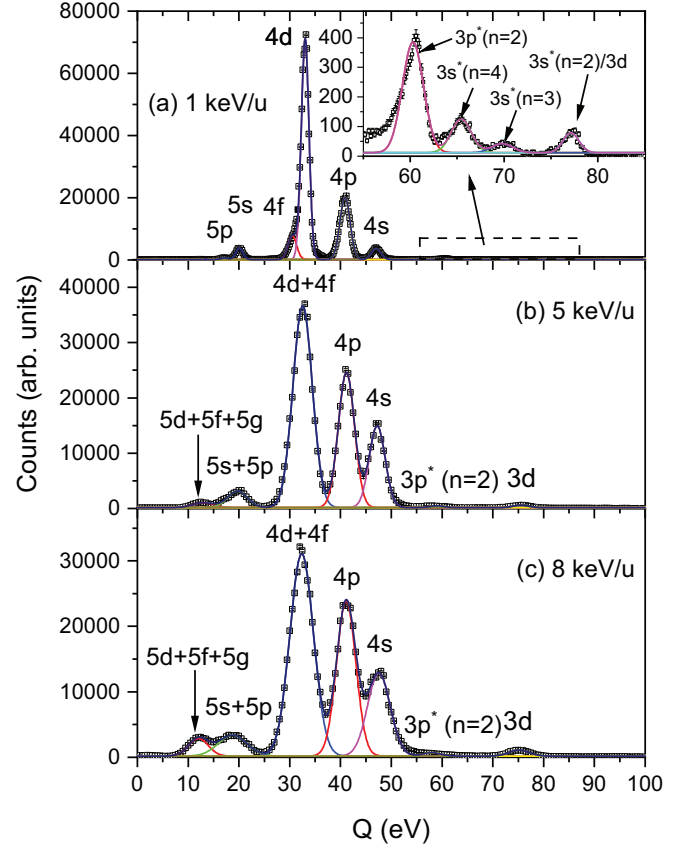

FIG. 1. Q-value spectra for the Ar^{8+}-He SC process at 1-, 5-, and 8-keV/u collision energies. For 1-keV/u collision energy, the Q-value spectrum from 55 to 85 eV is shown in the inset of panel (a).

decrease as the collision energy increases from 1 to 8 keV/u. This implies that the TE process is a two-step process where the projectile interacts with both electrons independently. Increasing the collision energy decreases the interaction time, resulting in reduced probability of the two-step process. Also, the excitation energies of the $He^+(n \geqslant 2)$ states are much higher, which requires a small impact parameter b collision to excite the electron in these states.

B. Angular distributions

Figure 2 shows the two-dimensional momentum density plots for the 1–8-keV/u Ar^{8+}-He SC process. The state-selective transverse momentum distributions reflect the rich oscillatory structures. With increasing collision energy, the spreads of the transverse profiles become narrower. In general small impact parameter collisions result in a large transverse momentum transfer and vice versa [9]. Clearly, the momentum density plot implies that the small impact parameter collisions are dominant at low collision energies. The interaction time is higher at 1-keV/u collision energy, and the electron can be adiabatically adapted to the small internuclear separation in the $ArHe^{8+}$ quasimolecular ions. The larger mean value of the transverse momentum distributions for the $3d$ and TE channels indicates that these states are populated through small b collisions.

TABLE I. Relative cross sections of the different final projectile states of $Ar^{7+}(n\ell)$ in the Ar^{8+}-He SC process at 1-, 5-, and 8-keV/u collision energies.

E (keV/u)	Final projectile states $Ar^{7+}(n\ell)$	Relative yields (%)
1	$5d + 5f + 5g$	0.12 ± 0.04
	$5p$	0.50 ± 0.03
	$5s$	3.05 ± 0.03
	$4f$	7.50 ± 0.19
	$4d$	61.28 ± 0.18
	$4p$	23.05 ± 0.26
	$4s$	3.77 ± 0.25
	$3d + 3s^*(n = 2)$	0.13 ± 0.01
	$3p^*(n = 2)$	0.48 ± 0.01
	$3s^*(n = 4)$	0.14 ± 0.01
	$3s^*(n = 3)$	0.04 ± 0.01
5	$5d + 5f + 5g$	1.32 ± 0.35
	$5s + 5p$	4.16 ± 0.34
	$4d + 4f$	49.63 ± 0.26
	$4p$	27.66 ± 0.25
	$4s$	16.38 ± 0.25
	$3d$	0.48 ± 0.18
	$3p^*(n = 2)$	0.50 ± 0.18
8	$5d + 5f + 5g$	3.20 ± 0.34
	$5s + 5p$	5.55 ± 0.38
	$4d + 4f$	44.39 ± 0.21
	$4p$	27.70 ± 0.27
	$4s$	17.50 ± 0.29
	$3d$	1.13 ± 0.25
	$3p^*(n = 2)$	0.57 ± 0.14

FIG. 2. Two-dimensional momentum density plots for (a) 1-, (b) 5-, and (c) 8-keV/u Ar^{8+}-He SC processes. The horizontal and vertical axes represent the recoil longitudinal and transverse momentum, respectively, in a.u. The color bar on the right side represents the counts in arbitrary units.

In order to gain insight into the ongoing charge-exchange dynamics, the state-selective DSADs have been unfolded. Figure 3 shows the state-selective DSADs for $1s$ to $4s$, $4p$, $4d$, and $4f$ transitions for the 1-keV/u SC process. For the simplest (i.e., $\Delta m_{fi} = 0$) $1s$ to $4s$ transition, experimentally obtained DSADs contain three oscillating lobes. The origin of these oscillations can be understood from the inelastic transition amplitude as given in Eq. (9), which contains a scattering amplitude and the Coulomb phase arising from the projectile-target relative motions. The state-selective scattering amplitude carries the nature of the electronic transition, while the projectile-target core interaction is augmented in the Coulomb phase factor. The scattering amplitudes are associated with the different impact parameters. For a defined impact parameter leading to a defined scattering angle, the different impact parameters b result in similar scattering angles that could interfere constructively or destructively, leading to coherent oscillations in the scattering angle distributions. For the other $\ell \neq 0$ transitions, i.e., $4p$, $4d$, and $4f$ states, different m-selective channels lead to different positions of maxima and minima, resulting in overall distributions. The TC-AOCC calculations show a good agreement for the dominant $1s$ to $4d$ transition and the smaller scattering angles for the $1s$ to $4f$ transition. A small shift in the TC-AOCC calculations has been observed for the $4s$ and $4p$ states. For both states (especially $4s$), TC-AOCC calculations overestimate the experimental differential cross sections at higher
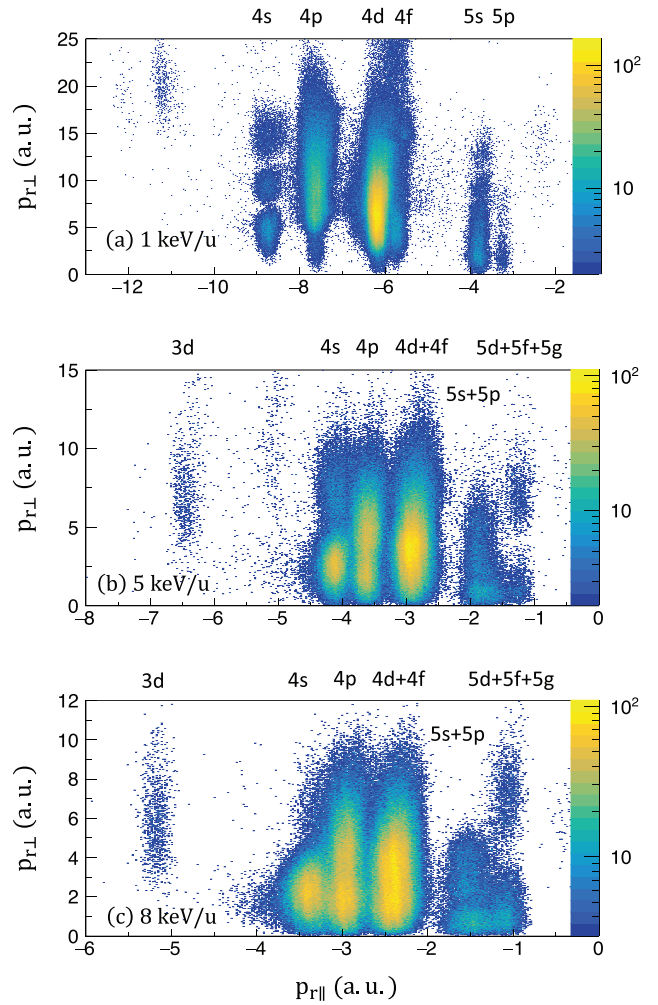
scattering angles, i.e., small b collisions. In the small b collisions (i.e., hard collisions), the interactions are mostly governed by complex molecular mechanisms where the electron-electron (e-e) correlations drastically influence the dynamics. On the other hand, the large b collisions (i.e., soft collisions) are mostly atomic transitions in nature. The effect of the e-e correlation is qualitatively understood as follows: The electronic Hamiltonian [see Eq. (4)] of the TC-AOCC calculation contains the attractive electron-projectile and the electron-target interactions. Meanwhile, the e-e correlation is a positive interaction. Therefore, without the e-e correlations in Eq. (4), the higher attractive interactions result in relatively close collisions, i.e., relatively higher scattering angles.

Figure 4 shows the DSADs for the $1s$ to $4s$, $4p$, and $4d+4f$ transitions for 5- and 8-keV/u SC collisions. The TC-AOCC calculations reproduced the oscillations in the measure DSADs for $1s$ to $4s$ transitions. Although there is a small shift towards the higher scattering angles, they mostly arise due to excluding the e-e correlation in the electronic Hamiltonian H. The transverse momentum distributions (see Fig. 2) already
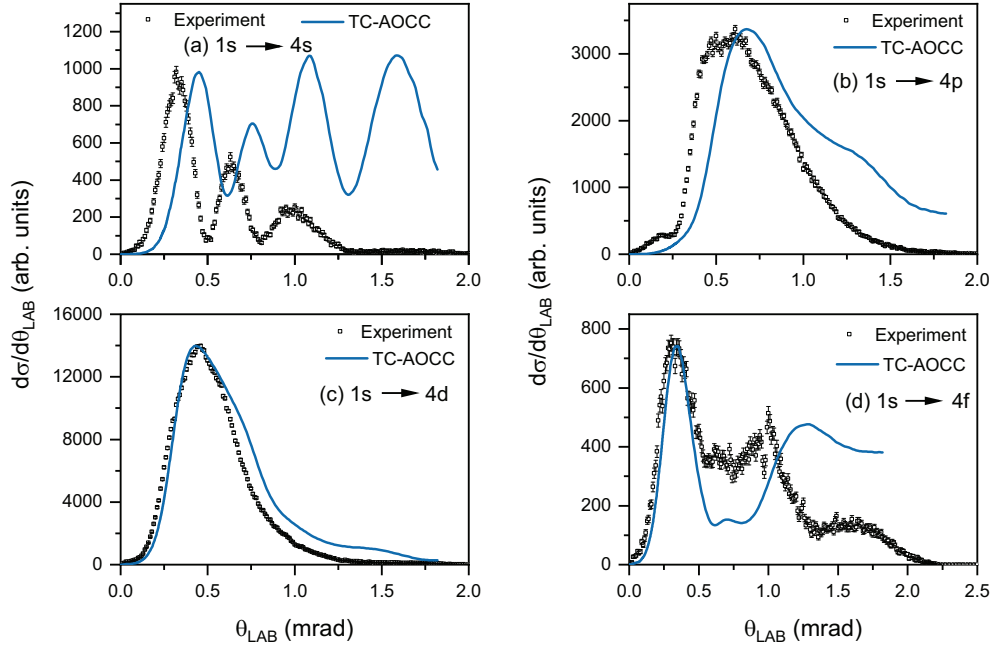
FIG. 3. DSADs of the state-selective electron capture for the $1s$ to $4s$, $4p$, $4d$, and $4f$ states for 1-keV/u Ar^{8+}-He collisions. The square symbols represent the experimental data, and the blue solid lines represent the TC-AOCC calculations. The TC-AOCC distributions are normalized with respect to the experimental counts.

show that with increasing collision energy, i.e., decreasing the interaction time, the small b collisions are not dominant as in the case of 1-keV/u energy. Therefore, relatively large b induced collisions give a better agreement where the molecularization effect is less.

Figures 4(b) and 4(e) show the DSADs for $1s$ to $4p$ transitions (solid lines) for 5- and 8-keV/u collision energies, respectively. At relatively low collision energy (i.e., 5 keV/u), the DSADs peak at the second oscillatory lobe, and the peak is shifted to the first oscillatory lobe when collision energy
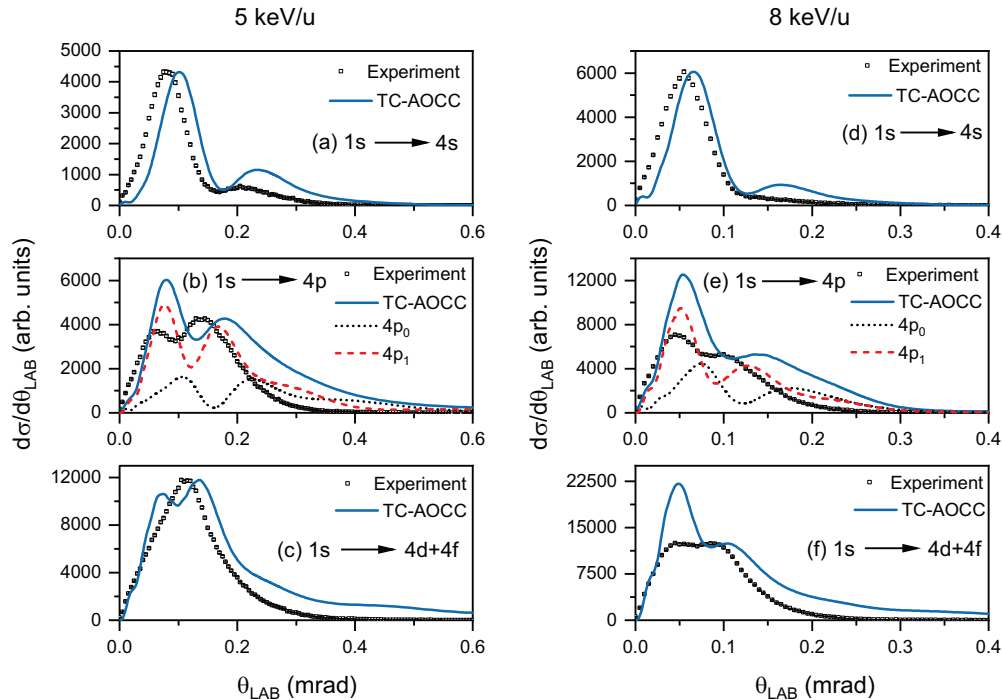

FIG. 4. DSADs of the state-selective electron capture for the $1s$ to $4s$, $4p$, and $4d + 4f$ states for 5-keV/u (a–c) and 8-keV/u (d–f) Ar^{8+}-He SC collisions. The square symbols represent the experimental data, and the blue solid lines represent the TC-AOCC calculations. The TC-AOCC data are normalized with respect to the experimental counts. Using the TC-AOCC calculations [see Eq. (8)], further m-selective DSADs for $1s$ to $4p_0$ (dotted lines) and $4p_1$ (dashed lines) have been unfolded for 5- and 8-keV/u collision energies (b, e).
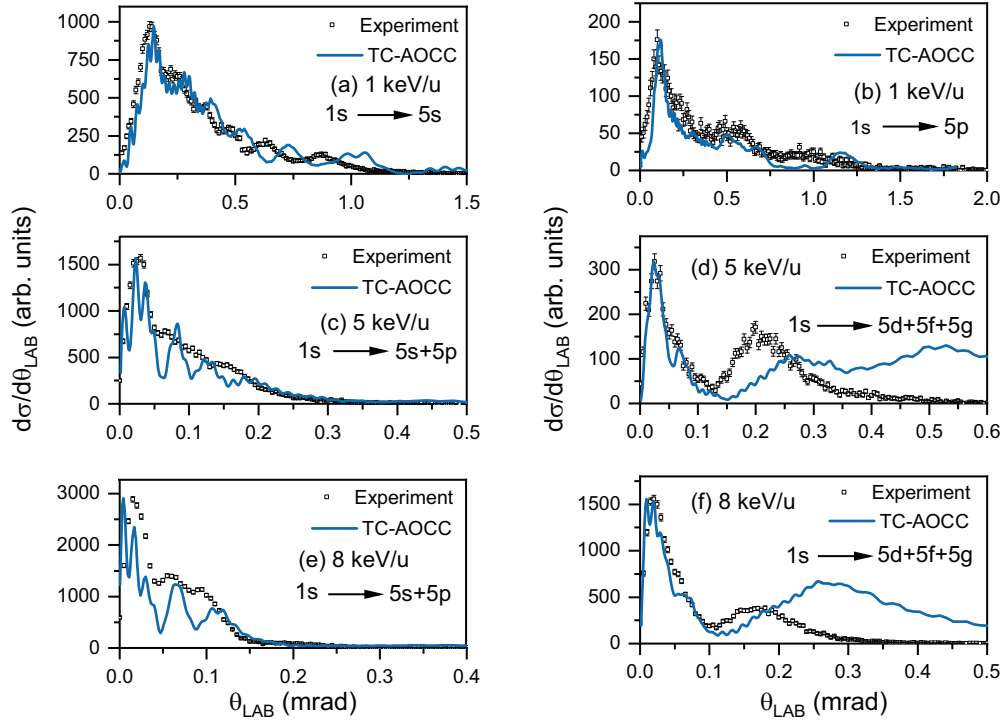
FIG. 5. DSADs of the state-selective electron capture for the $1s$ to 5ℓ states for 1-, 5-, and 8-keV/u Ar^{8+}-He collisions. The square symbols represent the experimental data, and the blue solid lines represent the TC-AOCC calculations. The TC-AOCC data are normalized with respect to the experimental counts.

increases to 8 keV/u. Qualitatively, this can be understood as that, in the quasimolecular picture, at a relatively lower collision energy, the small impact parameter b collisions dominate, resulting in larger scattering angles. We have already seen the dominance of the small b collisions in the transverse momentum distributions when the interaction time is higher (see Fig. 2).

As the collision velocities (i.e., $\upsilon \approx 0.45$ and 0.57 a.u.) are smaller than the orbital velocity ($\upsilon_e \approx 1.34$ a.u.) of the target electron, it forms an $ArHe^{8+}$ quasimolecular ion. The electronic cloud adapts adiabatically to the slow-moving nuclei, resulting in the different dynamical coupling effects [9,14,22]. In order to get an understanding of the dynamical coupling effects, the magnetic quantum number (m) selective DSADs for $1s$ to $4p_0$ and $4p_{\pm 1}$ transitions have been unfolded (magnetic quantum number superscript 1 is used for ± 1 unless otherwise stated). In brief, the dynamical coupling between the χ_k and χ_m states in a xz-collision plane can be written as [9]

$$\langle \chi_k | \frac{\partial}{\partial t} | \chi_m \rangle = \upsilon_R \langle \chi_k | \frac{\partial}{\partial R} | \chi_m \rangle + \frac{\upsilon b}{R^2} \langle \chi_k | iL_y | \chi_m \rangle, \quad (10)$$

where υ_R represents the radial velocity and L_y represents the projection of the angular momentum perpendicular to the collision plane xz. Here, $\langle \chi_k | \frac{\partial}{\partial R} | \chi_m \rangle$ and $\langle \chi_k | iL_y | \chi_m \rangle$ represent the radial coupling and rotational coupling, respectively. The radial coupling operator $\frac{\partial}{\partial R}$ couples the molecular states that have the same projection of the angular momentum on the internuclear axis, i.e., $\Delta m_{fi} = 0$ (e.g., $1s$ to $4p_0$ transition). The rotational coupling operator iL_y couples the states with the $\Delta m_{fi} = \pm 1$ (e.g., $1s$ to $4p_1$ transition). The rotational coupling dominantly occurs at small internuclear separations,

while the radial coupling starts to dominate with increasing collision velocity. Figures 4(b) and 4(e) show the m-selective DSADs for $1s$ to $4p_0$ (dotted lines) and $4p_1$ (dashed lines) transitions at 5- and 8-keV/u collision energies. The compari-
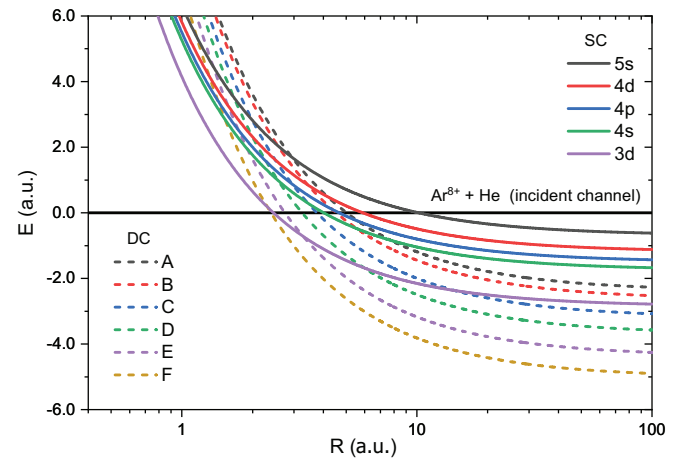

FIG. 6. Coulomb potential-energy curves for SC (solid lines) and DC (dashed lines) processes for Ar^{8+}-He collisions. The solid lines represent the outgoing channels for the state-selective $1s$ to $3d$, $4s$, $4p$, $4d$, and $5s$ transitions from left to right with increasing crossing radii. The dashed lines represent the DC channels for different Q values, i.e., A to F (see Sec. IV D for details). The straight black line at potential energy $V = 0$ indicates the incident Ar^{8+}+He capture channel. For simplicity, the polarization energy of the incident channel has been ignored.
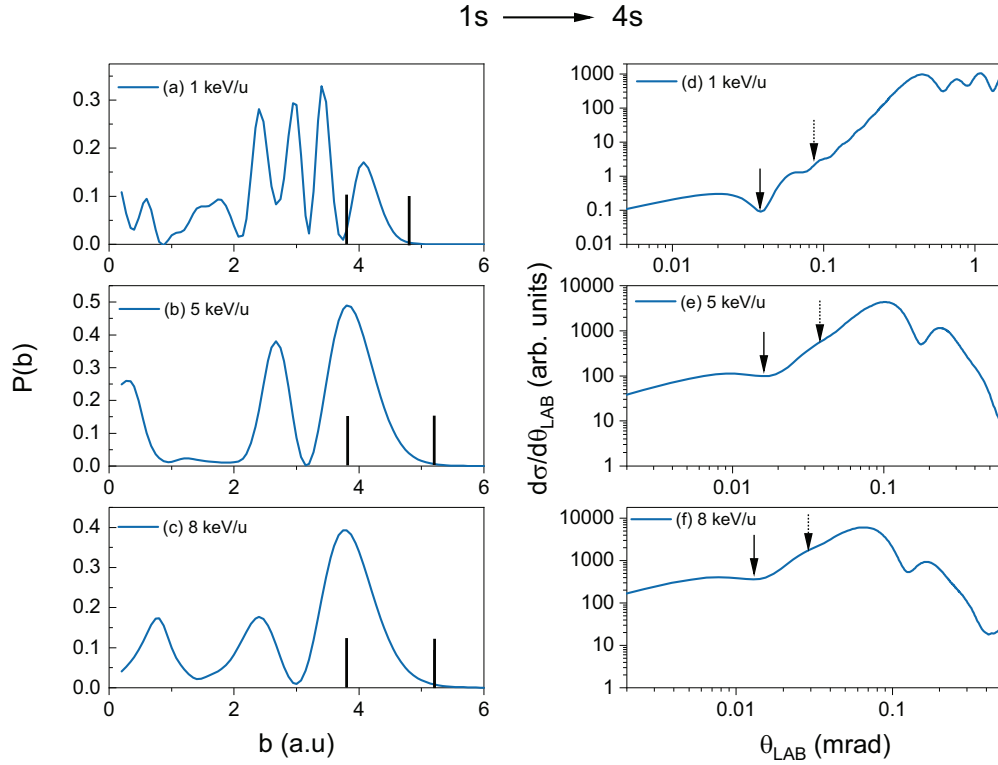
FIG. 7. The b-dependent $P(b)$ distributions (a–c) and the corresponding DSADs for the $1s$ to $4s$ (d–f) transitions are shown for the 1-, 5-, and 8-keV/u Ar^{8+}-He SC collisions. The ranges of the annular aperture (d–f) are indicated by the vertical solid black lines. The vertical solid and dotted arrows (d–f) represent the positions of the first and second diffraction minima estimated from the annular FDT model.

son between the experiment and TC-AOCC calculation for 5- and 8-keV/u $1s$ to $4p_1$ transition reflects that the simulation overestimates the first and the third oscillatory lobes. The exclusion of the e-e correlation overestimates the DSADs at smaller scattering angles, which is also confirmed by the two-electron active AOCC calculation [30].

Similar υ dependence DSADs have been observed in both experiment and simulation for $1s$ to $4d+4f$ transitions at 5- and 8-keV/u collision energy. The dominant peak of the DSADs shifted from a higher scattering angle (i.e., second oscillatory lobe) to a lower scattering angle (i.e., first oscillatory lobe) as relatively large b collisions start to dominate with increasing the collision energy from 5 to 8 keV/u. However, mixing of the $4d+4f$ states due to experimental resolution involved a large number of m-selective transitions (e.g., $4d_{0,1,2}$ and $4f_{0,1,2,3}$) unlike the $4p$ state.

Figure 5 shows the DSADs for the weakly populated and highly excited $1s$ to $n = 5\ell$ capture channels. For the 1-keV/u $1s$ to $5s$ transition, the measured DSADs contain six oscillations with decreasing intensity as scattering angles increase. The TC-AOCC calculation gives a good agreement except for a small shift due to the absence of e-e correlation. The $5p$ state also has several undulations but is not clearly distinguishable like the $5s$ state. The undulations in the $1s$ to $5s+5p$ transitions for both 5- and 8-keV/u collision energies are nearly reproduced by the TC-AOCC calculations. However, for the less populated $5d+5g+5f$ states, TC-AOCC calculations show an additional third oscillatory lobe at higher scattering angles, which is absent in the measure DSADs. It can be noted that

TC-AOCC calculation overestimates the higher scattering angles for weakly populated ℓ states for a corresponding n shell.

The measured DSADs for the $1s$ to $4s$ and $5s$ transitions at 1-keV/u collision energy consist of three and six oscillatory lobes, respectively (see Figs. 3 and 5). The scattering amplitude $A_{ji}(\theta)$ contains two oscillatory functions, i.e., $J_{|m_f-m_i|}$ and a_{fi} [see Eq. (8)]. It has been seen that the oscillations in DSADs are correlated with the oscillations in the probability distributions $P(b) = |a_{fi}|^2$ [30]. In the classical over-the-barrier picture, the Coulomb barrier is suppressed as the projectile approaches the target and forms a quasimolecular ion. In the quasimolecular picture, the electron is shared by both the projectile and the target. During this period, the electron can swap between the target and projectile, which results in the oscillations of the capture probability. The CPECs [38,39] estimate the associated capture radius (R_c), which depends inversely on the Q value for the same projectile (see Fig. 6). For the Ar^{8+}-He collision system, the R_c values for $4s$ and $5s$ states are ≈ 4 and ≈ 10 a.u., respectively. Therefore, the large interaction length (or interaction time) could lead to multiple swaps of the electron between the target and projectile during the interaction.

C. Quantum matter-wave diffraction

In order to get insight into undulations of DSADs that arise in the small scattering angles, a mathematical analysis based on the optical Fraunhofer diffraction of light has been introduced. Analogously to FDT of light, the differential cross
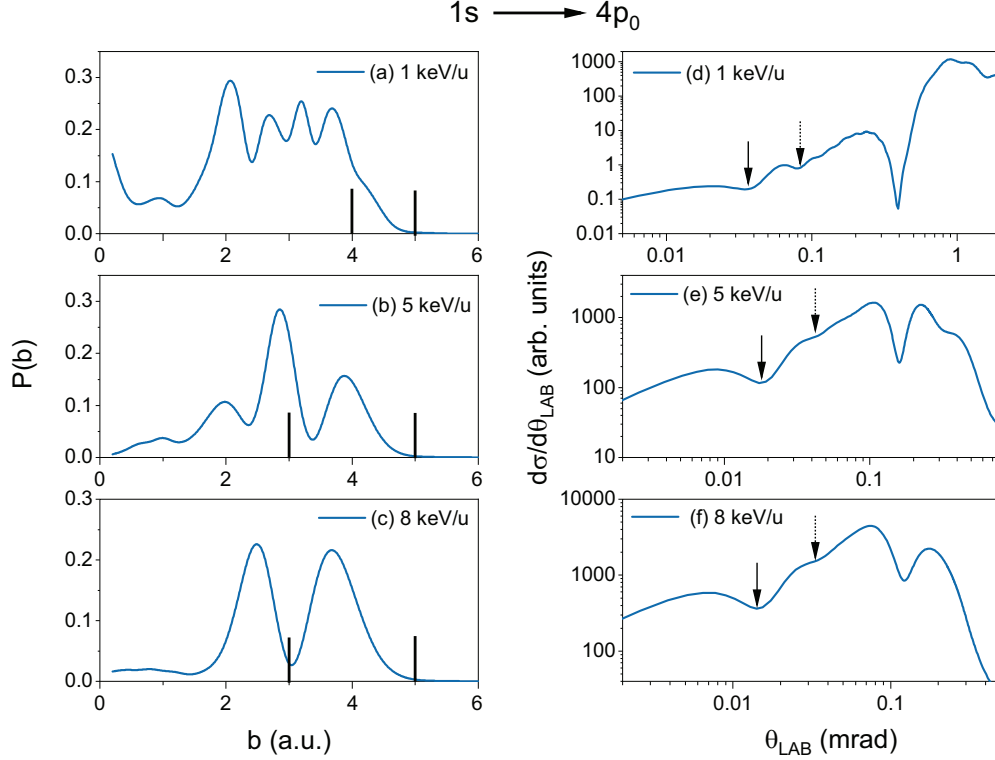
FIG. 8. The b-dependent $P(b)$ distributions (a–c) and the corresponding DSADs for the $1s$ to $4p_0$ (d–f) transitions are shown for the 1-, 5-, and 8-keV/u Ar^{8+}-He SC collisions. The ranges of the annular aperture (d–f) are indicated by the vertical solid black lines. The vertical solid and dotted arrows (d–f) represent the positions of the first and second diffraction minima estimated from the annular FDT model.

sections for $\Delta m_{fi} = 0$ transitions are given by

$$\frac{d\sigma}{d\Omega} \propto \left| \int_0^b b\,db\,F(b) J_0(kb \sin\theta) \right|^2, \quad (11)$$

where λ_{dB} ($k = 2\pi/\lambda_{dB}$) is the de Broglie wavelength of the incoming projectile.

In HCI-atom electron-capture collisions, the capture radius is generally large. The potential-energy curves of the quasi-molecular ions restrict the capture probability $P(b)$ near zero impact parameters. Therefore, the annular aperture gives a better physical picture of the b dependent $P(b)$ distributions. The optical FDT model shows that the intensity distributions for a uniform annular aperture of radii ϵa ($\epsilon < 1$) and a can be expressed as [40]

$$I(\theta) \propto \frac{1}{(1-\epsilon^2)^2} \left[\frac{2J_1(ka\sin\theta)}{ka\sin\theta}) - \epsilon^2 \frac{2J_1(ka\epsilon\sin\theta)}{ka\epsilon\sin\theta} \right]^2. \quad (12)$$

The impact parameter distributions and the FDT model results are shown in Figs. 7 and 8 with the TC-AOCC calculations for a uniform annular aperture.

We have tabulated the position of the diffraction fringes obtained from the TC-AOCC method and the annular FDT model for $1s$ to $4s$ and $4p_0$ transitions in Tables II and III, respectively. The FDT model roughly reproduced the positions of the dark and bright fringes with the theoretically calculated DSADs based on the TC-AOCC model. It can be seen that the b-dependent transition probabilities for $1s$ to $4s$ and $4p_0$ transitions are oscillating in nature in contrast to the simple

annular apertures (see Figs. 7 and 8). However, the FDT model for annular aperture gives an overall idea about the origin of these diffraction fringes arising from the large b collisions, i.e., soft collisions.

The Fraunhofer-type diffraction structures ride over smooth Gaussian-like distributions (see Figs. 7 and 8). The

TABLE II. Position of the diffraction fringes for the TC-AOCC theory deduced for $1s$ to $4s$ transition. The diffraction patterns for a uniform annular aperture (ρ_a) predicted by the FDT model are also tabulated.

Energy (keV/u)	Diffraction fringes	TC-AOCC (mrad)	FDT (mrad)
	ρ_a=3.8–4.8 a.u.		
1	First dark	0.038	0.038
	First bright		0.060
	Second dark	0.076	0.087
	Second bright		0.110
	Third dark	0.11	0.136
	ρ_a=3.8–5.2 a.u.		
5	First dark	0.016	0.016
	First bright		0.026
	Second dark		0.037
	ρ_a=3.8–5.2 a.u.		
8	First dark	0.013	0.013
	First bright		0.020
	Second dark		0.029

TABLE III. Position of the diffraction fringes for the TC-AOCC theory deduced for $1s$ to $4p_0$ transition. The diffraction patterns for a uniform annular aperture (ρ_a) predicted by the respective FDT model are also tabulated.

Energy (keV/u)	Diffraction fringes	TC-AOCC (mrad)	FDT (mrad)
	$\rho_a=4\text{–}5$ a.u.		
1	First dark	0.036	0.036
	First bright		0.058
	Second dark	0.080	0.083
	Second bright		0.105
	Third dark	0.115	0.130
	$\rho_a=3\text{–}5$ a.u.		
5	First dark	0.018	0.018
	First bright		0.028
	Second dark	0.044	0.042
	$\rho_a=3\text{–}5$ a.u.		
8	First dark	0.014	0.014
	First bright		0.022
	Second dark		0.033

DSADs are dominated by the oscillatory structures arising from the transition probability $P(b)$ oscillation and less contributions from the matter-wave scattering. In these slow, highly perturbative collisions, electronic dynamics is mostly governed by complex molecular mechanisms in the small b collisions through the avoided curve crossings. The different paths could interfere constructively or destructively, leading to coherent oscillations in the angular distributions. This kind of oscillation is known as a Stueckelberg-type oscillation and has been reported previously for the slow ion-atom collisions [41,42]. On the other hand, the matter-wave scattering is governed by the soft collisions arising from large b collisions. When the transition probability is smooth, i.e., not rapidly oscillating, the diffraction phenomena dominate [19,25]. It can be seen that the Stueckelberg-type oscillations have the dominant contributions over the Fraunhofer-type diffraction process in the highly perturbative HCI-atom collisions.

D. Ar^{8+}-He DC process

The principal quantum numbers for the SC (n) and DC (n') processes depend on the projectile charge q and the target ionization energy I_p for two independent electron-capture processes. The simple scaling laws [43,44] are as follows:

$$n \sim \frac{q}{\sqrt{2I_{p_1}\frac{q+2\sqrt{q}}{1+2\sqrt{q}}}} \quad (13)$$

and

$$n' \sim \frac{q}{\sqrt{2I_{p_2}\frac{q+2\sqrt{2q}}{2+2\sqrt{2q}}}}. \quad (14)$$

For He target, the I_p for first and second ionizations are 24.6 and 54.4 eV, respectively [45]. For the Ar^{8+}-He collision system, we have obtained $n \approx 4.15$ and $n' \approx 3.16$ from the above Eqs. (13) and (14). According to these scaling laws, the dominant final projectile states for the DC process can
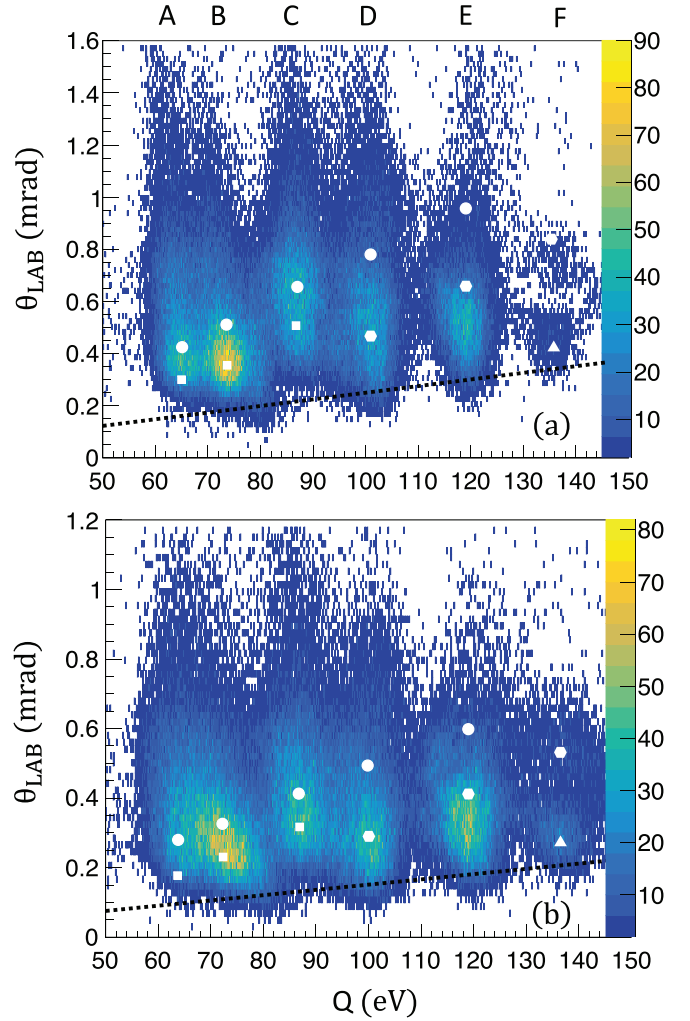

FIG. 9. Q-value (eV) vs scattering angle (mrad) distributions for (a) 5- and (b) 8-keV/u Ar^{8+}-He DC processes. The black dotted lines represent the Coulomb half-scattering angles for each collision energy. The solid circles, squares, hexagons, and triangles indicate the scattering angle values arising from the two-step DC process through $5s$, $4d$, $4s$, and $3d$ SC channels, respectively. The different Q-value peaks are labeled by A to F with increasing Q values. The color bar on the right side represents the counts in arbitrary units.

be represented as ($3\ell'4\ell$). We have presented the Q-value versus scattering angle distributions for 5- and 8-keV/u collision energies (see Fig. 9). Zhang *et al.* [32] show that the nonequivalent states ($n \neq n'$) dominate over the equivalent states ($n = n'$) in the DC process. At 5- and 8-keV/u collision energy, the relative cross sections of the projectile final states $3\ell'n\ell$ ($n > 5$), $3\ell'4\ell + 3\ell'5\ell$, and $3\ell'3\ell$ are nearly equivalent.

Generally, the nonequivalent states are populated in a two-step process where the projectile captures the electrons sequentially. This results in a higher scattering angle as the projectiles are deflected by Coulomb repulsion after capturing the first electron, and in order to capture the second electron the initial impact parameter should be smaller. On the other hand, in the single-step DC process, the projectile captures both electrons simultaneously in relatively higher impact parameters. Using the CPECs, one can estimate the

TABLE IV. Possible projectile final-state configurations $(n'\ell'n\ell)$ of the measured Q value for the Ar^{8+}-He DC process. The mean Q value and the width (full width at half maximum) are tabulated for A to F peaks. A few final projectile states are available in the NIST database, while a few are calculated using the flexible atomic code [46].

Peak	Q value (eV)	Projectile final states $(n'\ell'n\ell)$
A	64.4 ± 7.5	$3p7\ell + 3d4f + 3d4d$
B	73.2 ± 8.8	$3p5d + 3p6\ell$
C	86.9 ± 9.4	$3s6s + 3p5s + 3p4f$
D	100.6 ± 7.8	$3p4d + 3d^2$
E	118.9 ± 8.7	$3s4p$
F	136.1 ± 8.3	$3p3d$

crossing radii for the single-step and two-step electron-capture processes. Figure 6 shows the calculated Coulomb potential-energy curves for the Ar^{8+}-He SC and DC processes. Here, the single-step DC process occurs at an internuclear separation (R_{ss}) where the incoming channel (Ar^{8+}+He) crosses with the outgoing Ar^{6+}+He^{2+} channels. In the double-step DC process, the SC channels (Ar^{7+}+He$^+$) cross the DC channels at an internuclear separation (R_{ts}) smaller than the R_{ss}. For the single-step DC process, the estimated scattering angles from the CPECs are equivalent to the half-Coulomb scattering angle (θ_c), which is defined as

$$\theta_c = \frac{Q}{2E}, \qquad (15)$$

where E is the incident projectile energy.

Figure 9 shows the double differential Q-value vs scattering angle distributions for 5- and 8-keV/u Ar^{8+}-He true double-electron-capture processes. The black dotted lines show that the mean of the measured scattering angle distributions for almost all Q values is larger than the θ_c (see Fig. 9). This clearly indicates that both electrons are dominantly captured into the nonequivalent states of the Ar^{6+} $(n'\ell n\ell')$ final projectile ion. In order to get more clarity, we have calculated the scattering angles arising from the double-step DC process (see, e.g., Refs. [2,38,39]). For the two-step DC process, $3d$, $4s$, $4p$, $4d$, and $5s$ initial SC channels are considered. The estimated scattering angles indicate that the A and C Q-value peaks mostly arise from the SC through the $n\ell = 5\ell$ states while the B, D, and E peaks are induced through the $n\ell = 4\ell$ SC channels. A small contribution from the F peak is populated through the $n\ell = 3d$ SC channel. The capture radius for the $3d$ SC channel is smaller than the other $n\ell = 4\ell$ and 5ℓ channels, resulting in a smaller cross section. We have assigned the possible projectile final states corresponding to the measured Q values (i.e., A to F) in Table IV.

The different $n'\ell'n\ell$ states show overall Gaussian-like distributions in the state-selective DSADs except for the $3p3d$ state. Figure 10 shows the DSADs for the double-electron capture into the $3p3d$ state. The DSADs for 5-keV/u collision energy reveal three oscillatory lobes. With the increase in collision energy to 8 keV/u the third oscillatory lobe is suppressed. The sensitivity of the oscillations with the variation of the collision energy reflects a similar behavior to the SC
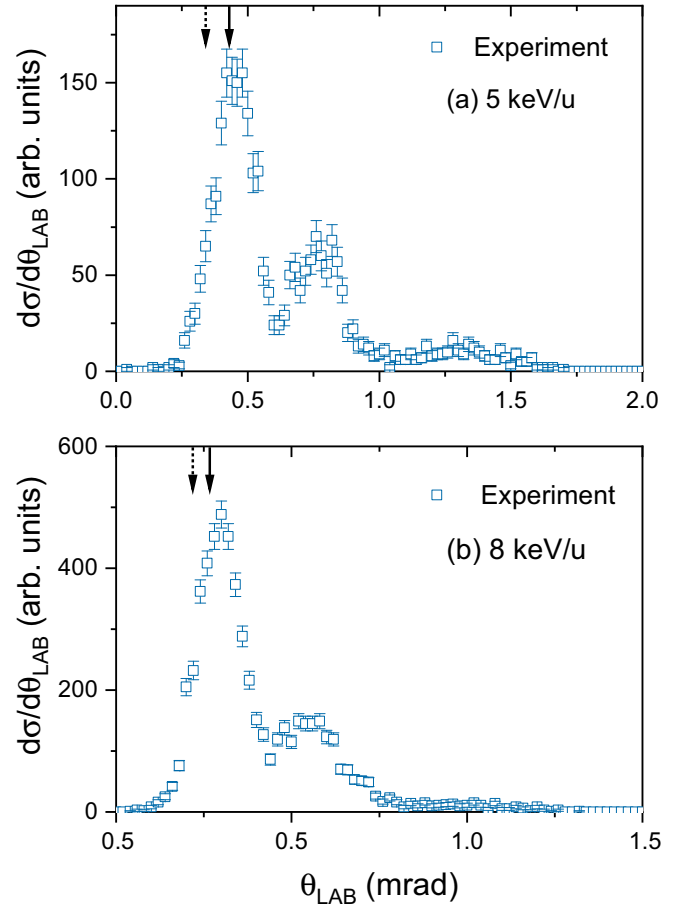

FIG. 10. DSADs of the state-selective double-electron capture for the $1s^2 \rightarrow 3p3d$ transition at 5- and 8-keV/u Ar^{8+}-He collisions. The dotted and solid arrows indicate the scattering angles associated with the single-step and double-step DC mechanisms through the $3d$ channel.

process (e.g., $1s \rightarrow 4s$ transition). This can be understood from the oscillating nature of the Coulomb phase, which is inversely proportional to the collision velocity. The oscillations are attributed to the Stueckelberg-type oscillations. It can also be seen that the DC into the $3p3d$ state via the single-step DC or double-step DC occurs in almost nearby capture radii (see Fig. 6). Therefore, the Coulomb deflections associated with these two processes do not differ much for this channel (see Fig. 10).

V. CONCLUSIONS

In conclusion, we present a comprehensive experimental study combined with theory for state-selective SC process in 1–8-keV/u Ar^{8+}-He collisions. The state-selective $(n\ell)$ partial cross sections indicate the dominant SC process takes place for $n = 4$ states and is weakly populated in $n = 5$ states. A small contribution from the TE channels at 1-keV/u collision energy implies that the two-step mechanism for this process increases with the increase in interaction time. The Stueckelberg-type oscillatory structures in the state-selective DSADs mostly arise from the interference between the scattering amplitudes. The oscillation periods that are increased

for highly excited states are explained by the electron swaps between the projectile and target nuclei in the quasimolecular picture. Shallow undulations in the DSADs at smaller scattering angles result from the quantum matter-wave scattering analogous to the optical Fraunhofer-type diffraction of light. A simple mathematical FDT model for an annular aperture further supports this finding.

For the Ar^{8+}-He DC process at 5–8-keV/u collision energies, electrons are transferred to the lower projectile states with high inelasticity (Q value around 65–150 eV). The double differential distributions between the Q values and the scattering angles indicate the DC process happens via the two-step process, resulting in large mean scattering angles. Our paper thus gives a physical insight into the role of quantum phenomena in characterizing the state-selective electron-capture dynamics for single- and double-electron-capture processes in strongly perturbative collisions.

[1] H. Knudsen, H. K. Haugen, and P. Hvelplund, Single-electron-capture cross-section for medium- and high-velocity, highly charged ions colliding with atoms, Phys. Rev. A **23**, 597 (1981).

[2] M. A. Abdallah, W. Wolff, H. E. Wolf, E. Y. Kamber, M. Stöckli, and C. L. Cocke, Single and double electron capture from He by Ar^{16+} studied using cold-target recoil-ion momentum spectroscopy, Phys. Rev. A **58**, 2911 (1998).

[3] M. A. K. A. Siddiki, K. Kumar, J. Mukherjee, L. C. Tribedi, and D. Misra, Role of the different electron capture processes in the molecular fragmentation dynamics in an Ar^{8+}-N_2 collision system, Phys. Rev. A **108**, 052805 (2023).

[4] H. Zettergren, H. T. Schmidt, P. Reinhed, H. Cederquist, J. Jensen, P. Hvelplund, S. Tomita, B. Manil, J. Rangama, and B. A. Huber, Even-odd effects in the ionization cross sections of $[C_{60}]_2$ and $[C_{60}C_{70}]$ dimers, Phys. Rev. A **75**, 051201(R) (2007).

[5] T. E. Cravens, X-ray emission from comets, Science **296**, 1042 (2002).

[6] P. Beiersdorfer, K. R. Boyce, G. V. Brown, H. Chen, S. M. Kahn, R. L. Kelley, M. May, R. E. Olson, F. S. Porter, C. K. Stahle, and W. A. Tillotson, Laboratory simulation of charge exchange-produced x-ray emission from comets, Science **300**, 1558 (2003).

[7] J. E. Rice, E. S. Marmar, J. L. Terry, E. Kallne, and J. Kallne, Observation of charge-transfer population of high-n levels in Ar^{16+} from neutral hydrogen in the ground and excited states in a tokamak plasma, Phys. Rev. Lett. **56**, 50 (1986).

[8] Y. Xue, R. Ginzel, A. Krauß, S. Bernitt, M. Schöffler, K. U. Kühnel, J. R. C. López-Urrutia, R. Moshammer, X. Cai, J. Ullrich, and D. Fischer, Kinematically complete study of electron transfer and rearrangement processes in slow Ar^{16+}-Ne collisions, Phys. Rev. A **90**, 052720 (2014).

[9] B. H. Bransden and M. R. C. McDowell, *Charge Exchange and the Theory of Ion-Atom Collisions* (Oxford University, New York, 1992).

[10] J. Ullrich and V. Shevelko, *Charge Exchange and the Theory of Ion-Atom Collisions* (Oxford University, New York, 1992).

[11] A. Leredde, A. Cassimi, X. Fléchard, D. Hennecart, H. Jouin, and B. Pons, Atomic-matter-wave diffraction evidenced in low-energy Na^++Rb charge-exchange collisions, Phys. Rev. A **85**, 032710 (2012).

[12] C. H. Liu, J. G. Wang, and R. K. Janev, Single- and double-charge transfer in slow He^{2+}-He collisions, J. Phys. B **45**, 235203 (2012).

[13] W. Fritsch, Theoretical study of electron processes in slow He^{2+}-He collisions, J. Phys. B **27**, 3461 (1994).

[14] R. T. Zhang, X. L. Zhu, X. Y. Li, L. Liu, S. F. Zhang, W. T. Feng, D. L. Guo, Y. Gao, D. M. Zhao, J. G. Wang, and X. Ma, Single-electron capture in 3-keV/u Ar^{8+}-He collisions, Phys. Rev. A **95**, 042702 (2017).

[15] X.-M. Tong, D. Kato, T. Watanabe, and S. Ohtani, Time-dependent Schrödinger equation method: Application to charge transfer and excitation in H and H^+ collisions, Phys. Rev. A **62**, 052701 (2000).

[16] R. Dörner, V. Mergel, O. Jagutzki, L. Spielberger, J. Ullrich, R. Moshammer, and H. Schmidt-Böcking, Cold target recoil ion momentum spectroscopy: A momentum microscope to view atomic collision dynamics, Phys. Rep. **330**, 95 (2000).

[17] J. Ullrich, R. Moshammer, A. Dorn, R. Dörner, L. P. H. Schmidt, and H. Schmidt-Böcking, Recoil-ion and electron momentum spectroscopy: Reaction-microscopes, Rep. Prog. Phys. **66**, 1463 (2003).

[18] M. A. Abdallah, W. Wolff, H. E. Wolf, E. Sidky, E. Y. Kamber, M. Stöckli, C. D. Lin, and C. L. Cocke, Cold-target recoil-ion-momentum spectroscopy study of single electron capture from He by slow Ar^{8+} ions, Phys. Rev. A **57**, 4373 (1998).

[19] M. Gudmundsson, D. Fischer, N. Haag, H. A. B. Johansson, D. Misra, P. Reinhed, H. Schmidt-Böcking, R. Schuch, M. Schöffler, K. Støchkel, H. T. Schmidt, and H. Cederquist, Angular scattering in fast ion-atom electron transfer collisions: Projectile wave diffraction and Thomas mechanisms, J. Phys. B **43**, 185209 (2010).

[20] T. G. Winter, G. J. Hatton, and N. F. Lane, Molecular-state treatment of collisions between protons and He^+ ions, Phys. Rev. A **22**, 930 (1980).

[21] A. Dubois, S. E. Nielsen, and J. P. Hansen, State selectivity in H^+-Na (3s/3p) collisions: Differential cross sections, alignment and orientation effects for electron capture, J. Phys. B **26**, 705 (1993).

[22] N. Andersen, J. T. Broad, E. E. Campbell, J. W. Gallagher, and I. V. Hertel, Collisional alignment and orientation of atomic outer shells. II. Quasi-molecular excitation, and beyond, Phys. Rep. **278**, 107 (1997).

[23] M. van der Poel, C. V. Nielsen, M.-A. Gearba, and N. Andersen, Fraunhofer diffraction of atomic matter waves: Electron transfer studies with a laser cooled target, Phys. Rev. Lett. **87**, 123201 (2001).

[24] M. van der Poel, C. V. Nielsen, M. Rybaltover, S. E. Nielsen, M. Machholm, and N. Andersen, Atomic scattering in the diffraction limit: Electron transfer in keV Li$^+$-Na(3s, 3p) collisions, J. Phys. B: At. Mol. Opt. Phys. **35**, 4491 (2002).

[25] H. Agueny, Fraunhofer-type diffraction patterns of matter-wave scattering of projectiles: Electron transfer in energetic ion-atom collisions, Phys. Rev. A **92**, 012702 (2015).

[26] D. L. Guo, J. W. Gao, S. F. Zhang, X. L. Zhu, Y. Gao, D. M. Zhao, R. T. Zhang, Y. Wu, J. G. Wang, A. Dubois, and X. Ma, State-selective single-electron capture in intermediate-energy C^{4+}+ He collisions, Phys. Rev. A **103**, 032827 (2021).

[27] M. A. K. A. Siddiki, J. Mukherjee, K. Kumar, K. Tőkési, D. Misra, and H. Agueny, Observing quantum matter-wave diffraction in the energetic He^{2+}-He collisions, Phys. Rev. Res. **6**, 013108 (2024).

[28] M. A. K. A. Siddiki, G. P. Zhao, L. Liu, and D. Misra, Highly excited quantum state-selective capture dynamics in slow Ar^{8+}-H_2 collisions, Phys. Rev. A **109**, 032819 (2024).

[29] M. Druetta, S. Martin, T. Bouchama, C. Harel, and H. Jouin, Spectroscopic study of the charge-exchange collision between Ar^{8+} and He or H_2 at beam energies of 80, 40, and 8 keV, Phys. Rev. A **36**, 3071 (1987).

[30] R. T. Zhang, J. W. Gao, Y. W. Zhang, D. L. Guo, Y. Gao, X. L. Zhu, J. W. Xu, D. M. Zhao, S. Yan, S. Xu, S. F. Zhang, Y. Wu, J. G. Wang, and X. Ma, Strongly perturbed state-selective charge exchange between slow Ar^{8+} and He, Phys. Rev. Res. **5**, 023123 (2023).

[31] S. Bliman, M. Cornille, B. A. Huber, and J. F. Wyart, Double-electron capture and population of Rydberg levels in slow Ar^{8+} + He collisions, Phys. Rev. A **56**, 4683 (1997).

[32] Y. W. Zhang, J. W. Gao, Y. Wu, J. G. Wang, N. Sisourat, and A. Dubois, Single- and double-electron capture in intermediate-energy Ar^{8+}+ He collisions, Phys. Rev. A **106**, 042809 (2022).

[33] A. N. Agnihotri, A. H. Kelkar, S. Kasthurirangan, K. V. Thulasiram, C. A. Desai, W. A. Fernandez, and L. C. Tribedi, An ECR ion source-based low-energy ion accelerator: Development and performance, Phys. Scr. **T144**, 014038 (2011).

[34] M. A. K. A. Siddiki, M. Nrishimhamurty, K. Kumar, J. Mukherjee, L. C. Tribedi, A. Khan, and D. Misra, Development of a cold target recoil ion momentum spectrometer and a projectile charge state analyzer setup to study electron transfer processes in highly charged ion-atom/molecule collisions, Rev. Sci. Instrum. **93**, 113313 (2022).

[35] M. A. K. A. Siddiki, L. C. Tribedi, and D. Misra, Probing the fragmentation pathways of an argon dimer in slow ion-dimer collisions, Atoms **11**, 34 (2023).

[36] A. Khan, L. C. Tribedi, and D. Misra, A recoil ion momentum spectrometer for molecular and atomic fragmentation studies, Rev. Sci. Instrum. **86**, 043105 (2015).

[37] L. Liu, C. H. Liu, J. G. Wang, and R. K. Janev, Cross sections for electron capture in H^+-$Li(2p\sigma, \pi^{\pm})$ collisions, Phys. Rev. A **84**, 032710 (2011).

[38] P. Roncin, M. Barat, and H. Laurent, Differential cross-sections for one- and two-electron capture by highly charged ions (N^{7+}, O^{7+}, O^{8+}, Ne^{7+}, Ne^{8+}) at low keV energies, Europhys. Lett. **2**, 371 (1986).

[39] H. Laurent, M. Barat, M. N. Gaboriaud, L. Guillemot, and P. Roncin, Differential cross sections and electron transfer mechanisms in multiply charged ion-atom collisions, J. Phys. B **20**, 6581 (1987).

[40] M. Born and E. Wolf, *Principles of Optics: Electromagnetic Theory of Propagation, Interference, and Diffraction of Light* (Elsevier, Amsterdam, 2013).

[41] A. Barany, H. Danared, H. Cederquist, P. Hvelplund, H. Knudsen, J. O. K. Pedersen, C. L. Cocke, L. N. Tunnell, W. Waggoner, and J. P. Giese, Stueckelberg angular scattering oscillations in two-electron capture by C^{4+} from He at low energies, J. Phys. B **19**, L427 (1986).

[42] R. E. Olson and F. T. Smith, Collision spectroscopy. IV. Semi-classical theory of inelastic scattering with applications to He^+ + Ne, Phys. Rev. A **3**, 1607 (1971).

[43] H. Ryufuku, K. Sasaki, and T. Watanabe, Oscillatory behavior of charge transfer cross sections as a function of the charge of projectiles in low-energy collisions, Phys. Rev. A **21**, 745 (1980).

[44] D. L. Guo, R. T. Zhang, X. L. Zhu, Y. Gao, K. Z. Lin, T. Cao, D. M. Zhao, X. B. Zhu, C. J. Zhang, S. F. Zhang, and X. Ma, Benchmark $n\ell$-resolved cross sections of single and double charge exchange processes in 1.67–20 keV/u C^{4+} collisions with He, Astrophys. J. **941**, 31 (2022).

[45] NIST: Atomic Spectra Database, Energy Levels, https://physics.nist.gov/PhysRefData/ASD/levels_form.html.

[46] M. F. Gu, The flexible atomic code, Can. J. Phys. **86**, 675 (2008).